4-2020

Detailed Modeling of a Small-Scale Turbulent Pool Fire

Bifen Wu
University of Connecticut - Storrs

Somesh Roy
Marquette University, somesh.roy@marquette.edu

Xinyu Zhao
University of Connecticut - Storrs

Recommended Citation

Wu, Bifen; Roy, Somesh; and Zhao, Xinyu, "Detailed Modeling of a Small-Scale Turbulent Pool Fire" (2020). *Mechanical Engineering Faculty Research and Publications*. 250.
https://epublications.marquette.edu/mechengin_fac/250

Mechanical Engineering Faculty Research and Publications/College of Engineering

Combustion and Flame, Vol. 214 (April 2020): 224-237. DOI. This article is © Elsevier and permission has been granted for this version to appear in e-Publications@Marquette. Elsevier does not grant permission for this article to be further copied/distributed or hosted elsewhere without the express permission from Elsevier.

Detailed Modeling of a Small-Scale Turbulent Pool Fire

Bifen Wu
Department of Mechanical Engineering, University of Connecticut, Storrs CT
Somesh P. Roy
Department of Mechanical Engineering, Marquette University, Milwaukee WI
Xinyu Zhao
Department of Mechanical Engineering, University of Connecticut, Storrs CT

Abstract

Turbulent pool fires have been studied as a canonical configuration in fire science with wide interest. A numerical study of a small-scale turbulent heptane pool fire is conducted in the present study to understand the interactions and coupling among turbulence, chemistry, soot, and radiation in pool fires. A Monte Carlo ray tracing based radiation solver, with line-by-line spectral models for five gaseous species and soot, is coupled with a fireFOAM-based reacting flow solver to describe the dynamics of the target fire. A 33-species skeletal mechanism is employed to describe the finite-rate chemistry. A two-equation soot model with C_2H_2 based inception model is incorporated to describe soot dynamics. Turbulence is resolved by the computational grid to avoid the uncertainties in modeling the sub-grid scale stress and turbulence-chemistry-radiation interactions. The computed radiative heat fluxes are directly compared with experimental signals and good agreement is observed. Rarely compared in the literature, the line-of-sight spectral distribution of the emissive power is computed and compared with experimental measurements with excellent match in the 4300 nm CO_2-dominant emissive peak. A secondary emissive peak near 3300 nm is absent from the numerical results, which can be attributed to experimental uncertainties and/or insufficient representation of the C-H stretching bonds in the radiation spectral model. The instantaneous flame structures show the presence of abundant hydrocarbon molecules as fuel pyrolysis products. A detailed examination of the chemical and radiative source terms reveals the disproportionate relation between these two source terms, especially when soot is present. Soot radiation is largely optically thin while gas radiation is much thicker in optical depth, as a result of the spatial structures of the flame and the non-grey interactions between gas and soot. With the abundant information provided by the detailed simulation in this study, models for turbulence-chemistry-radiation interactions will be derived in future work.

Keywords

Pool fire, Monte Carlo ray tracing, Two-equation soot model, Line-by-line

1. Introduction

Turbulent pool fires have been widely studied for decades [1], as one of the canonical configurations in fire science. Turbulent pool fires of different scales and with various fuels have been employed to investigate fire dynamics [1], [2], thermal radiation [3], fuel burning rate [4], and extinction [5], [6]. Experimental efforts are constantly leveraged to investigate the fundamental physics identified above and to validate numerical models. Dating back to 1970s, McCaffrey [7] measured flame temperatures and vertical velocities along the centerline of methane pool fires. Since then, the empirical correlations of temperature and velocity established based on experiments have been used widely for verification and validation in pool fire studies [8], [9]. To extend the understanding of radiation characteristics in all regions of pool fires, Klassen and Gore [10] studied the burning rate, radiative loss, emissive and absorption temperatures, and flame heights for liquid pools ranging from 4.6 to 100 cm in diameter. The abundant radiation-relevant data have been widely adopted to assess radiation models [11], [12]. However, local measurements of other combustion-relevant quantities, such as temperature and species concentrations, were often missing in this collection of experimental measurements. Weckman and Strong [13] measured the radial velocity and temperature at different elevations downstream of a medium-scale methanol pool fire to investigate the complex mixing and entrainment patterns. The dynamics of these methanol pool fires is relatively less impacted by radiation, and they are often employed to validate sub-grid fluid dynamics models [14], [15]. Comprehensive reviews of suitable experiments for validating numerical methods are provided in [4], [16]. A more recent model validation framework and associated experimental and numerical databases are available in [17], [18].

With the aid of these experimental databases and rapid advancement of high performance computing, large eddy simulations (LES) have been applied to turbulent pool fires to understand different pertinent physical processes since early 2000s [9], [11], [14], [15], [19], [20]. For example, Xin*et al*. [11]

performed LES of a 7.1 cm methane pool fire using a mixture fraction based combustion model and a single-step kinetic model. Radiation was modeled by a fixed radiant fraction, where radiative loss is constantly proportional to the local chemical heat release rate. Subsequently, Xin *et al*. [21] extended the developed solver to simulate a one-meter diameter methane pool fire. The performances of two radiation models, one is the aforementioned fixed radiant fraction method and the other is a finite volume method (FVM) with grey radiative properties, were compared. They noticed that ignoring radiative heat loss leads to an over-prediction of vertical velocity. Almeida *et al*. [12] further adopted the discrete ordinates method based on the finite volume implementation (fvDOM) to simulate the same 7.1 cm methane pool. The grey media assumption and the Planck mean absorption coefficient were used to describe the radiative properties. The eddy dissipation combustion model (EDM) was combined with a single-step reaction to close the sub-grid scale reaction rate. Comparing with experiments, they overestimated the radiant fraction and suggested that improved radiation models should be included.

To improve the predictive capability of numerical models, many studies have attempted to go beyond empirical correlations and to incorporate more robust sub-models for turbulence, chemistry, radiation, and soot, etc. For example, Cheung and Yeoh [22] conducted a fully-coupled LES of a large-scale methane pool fire. The strained laminar flamelet approach combined with a single-step reaction was used to consider turbulence-chemistry interactions (TCI). To account for soot dynamics, a two-equation soot model [23] that relates soot production to the local temperature and fuel mole fraction was adopted. Radiation was solved by the discrete ordinates method (DOM) with the S4 quadrature scheme and with a weighted-sum-of-grey-gas (WSGG) model. With these submodels, they quantitatively captured velocity fluctuations and the pulsation frequency. More recently, Maragkos *et al*. [14] systematically studied a 30.5 cm methanol pool fire. A single-step kinetic model and a fixed radiant fraction model were used for chemistry and radiation, respectively. Through experimental validation and parametric studies, they concluded that the non-unity Lewis number model has a discernible impact on the prediction of flame temperature. Prediction of the flow field is also improved with the dynamic turbulence model compared to the one-equation eddy viscosity model [24]. In a subsequent study, Maragkos *et al*. [15] incorporated the WSGG model for radiation, and compared their latest results against the experimental data. The use of the WSGG model accurately reproduced the experimental radiatnt fraction, which suggests the importance of more accurate radiation models. Besides the above submodels, soot modeling becomes critical for heavily sooting pool fires. Chatterjee *et al*. [9] developed a combined sub-grid soot-radiation model, based on the laminar smoke point concept [25], and applied it to a 30 cm heptane pool fire. Good agreement with the McCaffrey correlation [7] was attained for the mean centerline temperature rise and velocity, due to the inclusion of soot and radiation. Very recently, Snegirev *et al*. [26] compared the performances of several soot models, such as the one-step model by Khan *et al*. [27], the two-step model By Tesner*et al*. [28], and the Moss-Brookes model [29], in a 30 cm pool fire fueled by methane and heptane, respectively. These soot models predicted dramatically different distributions of soot volume fractions both inside the flame and in the overfire region, which suggests that a suitable soot model with careful calibration for fire modeling is essential.

Despite the progress made in simulating and capturing the multi-physical interactions, robustly modeling pool fires remains challenging, especially when new physics is introduced. Suppression conditions such as reduced ambient oxygen contents can easily break models that cannot account for extinction physically. Discrete ordinates methods have seen dominance in modeling radiation in fire, however, the accuracy of the solver is sensitive to the quality of spatial discretization, the associated spectral models, and the participative media involved (e.g., whether scattering exists). In addition, significant uncertainties still persist in soot models and chemical kinetic models, as discussed in [30], [31]. Lastly, appropriate turbulence-chemistry-radiation interactions models are currently under active development [32], posing further challenges to LES of pool fires.

To this end, the present study seeks to improve the understanding of radiation, chemistry, soot, and turbulence interactions in turbulent pool fires through high-fidelity simulations. Uncertainties in modeling radiation and turbulence-radiation-chemistry interactions are mitigated by invoking a line-by-line Monte Carlo ray tracing (MCRT) radiation solver [33] and a turbulence-resolved grid. A 33-species finite-rate kinetic model [34] is employed to robustly account for various chemical properties of the system, such as flame ignition and propagation. Soot formation and oxidation are accounted for through a semi-empirical two-equation soot model. Unlike the combined soot-radiation model in [9], the radiative effect of soot is considered separately by the aforementioned radiation solver. To the best of authors' knowledge, the current study incorporates the most comprehensive physical details in modeling pool fires, the numerical instrumentation of which is also a challenge in order to maintain reasonable computational cost.

The rest of the paper is organized as follows. The modeling framework is first introduced in Section 2, followed by the details of the target turbulent heptane pool fire in Section 3. In Section 4, results obtained from coupled combustion-radiation simulations are presented and discussed with a particular focus on the thermochemical characteristics of the target fire. Conclusions are finally drawn in Section 5.

2. Methodology

The simulations are conducted using the *reactingDJFoam* solver [35], which is constructed using components of fireFoam [36] and in-house chemistry and radiation solvers. The coupled transport equations for mass, momentum, species mass fractions, and sensible enthalpy are solved by a segregated pressure-based finite volume method. A pressure Poisson equation is solved with the momentum equation using a pressure-implicit with splitting of operators (PISO) algorithm [37]. The *reactingDJFoam* solver has been systematically verified using zero-dimensional (0D) auto-ignition reactor and one-dimensional (1D) unstrained laminar premixed flames in [35], two-dimensional (2D) axisymmetric laminar coflow flames in [38], and three-dimensional (3D) turbulent premixed flames in [35], where satisfactory agreements with experiments were achieved. Readers can refer to Ref. [35] for details of the governing equations. Key features of the solver are briefly reviewed in Section 2.1. Subsequently, radiation and soot models are described in Sections. 2.2 and 2.3, respectively.

2.1. The numerical solver

A mixture-averaged molecular transport property model [39] has been implemented into *reactingDJFoam* to account for the non-unity Lewis and Schmidt numbers effects, which is critical for modeling pool fires with heavy hydrocarbon fuels [14]. Pool fires often transition from laminar to turbulent from upstream to downstream, and the mixture-averaged molecular transport model is expected to be adequate for both the laminar and turbulent regions of the flame. The non-unity Lewis and Schmidt number effects are also expected to be non-negligible for modeling turbulent flames in well-resolved LES, as is the case in the present study.

A 33-species, 227-reactions n-heptane skeletal mechanism [34] is employed to account for the finite-rate chemistry. This model was systematically reduced from JetSurf v1 [40] to predict both pyrolysis and oxidation of n-heptane for high-temperature applications. The skeletal mechanism showed good agreement with the detailed mechanism for ignition delay, laminar flame speed, and extinction residence time [34]. To further assess the accuracy of the skeletal mechanism in preserving the structures of radiation-relevant species, the mass fractions of CO_2, H_2O, CO, CH_4 and C_2H_4, are computed from the detailed and skeletal mechanisms using a non-premixed laminar counterflow flame, as shown in Appendix A. Profiles in the mixture fraction space are compared, and the maximum difference is approximately 6.8%, observed for the peak mass fraction of C_2H_4 at $Z = 0.234$. Therefore, the skeletal mechanism is considered to be sufficiently accurate in capturing both chemistry and radiation-relevant species in this study.

Note that global reactions are usually employed for fire modeling. The 33-species mechanism enables application of C_2H_2 based semi-empirical soot models. It also allows for quantification of radiation characteristics from participating species such as C_2H_4, CH_4, and other hydrocarbons. To accelerate the integration of chemical source terms, the adaptive hybrid integration solver with sparse matrix technique (AHI-S) presented in [35] is employed.

2.2. Thermal radiation modeling

2.2.1. Solver and spectral models

The radiation transfer equation (RTE) is solved via a Monte Carlo ray tracing (MCRT) solver [41], [42], [43]. The MCRT method solves the RTE by emitting and tracking a statistically large number of "energy rays" to account for their interactions with participating media [41], [42]. Each energy ray carries a specific amount of energy and has a specific wavenumber, direction, and origin. They are emitted everywhere within the computational domain by the participating gases, soot, and hot walls. The power of each energy ray is proportional to the local emission potential of its host cell, and is inversely proportional to the number of rays emitted from the same cell. The selection algorithms of the origin, propagation direction, and wavenumber of each energy ray are based on the random number relations that have been established in [41], [44]. As each ray moves through the domain, it loses energy due to absorption, and changes direction due to scattering along its travel path. Each energy ray is tracked until its energy is completely absorbed by the participating media or it hits and/or exits the computational boundaries. Once the ray tracing is completed, the total radiative source term, S_r, can be collected for each computational cell and the radiative heat flux can be collected for the boundary. The volumetric radiative source can be expressed as,

$$S_r = Q_{emi} - Q_{abs} = 4\kappa_P \sigma T^4 - Q_{abs} \quad (1)$$

where Q_{emi} and Q_{abs} are the volumetric emission and absorption source terms, respectively. For a mixture where both soot and gases are present, the pressure based total Planck-mean absorption coefficient can be computed as

$$\kappa_P = \kappa_{P,g} + \kappa_{P,s} \quad (2)$$

The Planck-mean absorption coefficient $\kappa_{P,g}$ for gases is defined as,

$$\kappa_{P,g} = \frac{\int_0^{\infty} \kappa_\nu I_{b\nu} d\nu}{\int_0^{\infty} I_{b\nu} d\nu} \quad (3)$$

where ν is the wavenumber, and $I_{b\nu}$ is the blackbody emissive intensity evaluated at wavenumber ν. κ_ν is the absorption coefficient at wavenumber ν, and it takes the following additive form when more than one participating gaseous species are present,

$$\kappa_\nu = \sum_i \kappa_{p\nu,i} p_i \quad (4)$$

Here, p_i is partial pressure of species i, and $\kappa_{p\nu,i}$ is the pressure-based spectral absorption coefficient for species i at wavenumber ν.

The pressure-based spectral absorption coefficients are obtained from the line-by-line (LBL) database [44] that is generated from HITEMP2010 [45] and HITRAN2012 [46]. Five species, including CO_2, CO, H_2O, CH_4 and C_2H_4, are considered for temperatures from 300 K to 3000 K, and for various mole fractions of the participating species. It should be noted that the spectral databases for hydrocarbons such as CH_4 and C_2H_4 are constantly updated as demonstrated by the effort from the HITRAN community [46]. For the purpose of accounting for thermal radiation, the line-by-line databases are sufficiently accurate and have been regarded as the “truth” for spectral model development. For soot, the Planck-mean absorption coefficient, $\kappa_{P,s}$, is evaluated using a similar method as Eq. (3), where the spectral absorption coefficient κ_ν is replaced by $\kappa_{\nu,s}$. $\kappa_{\nu,s}$ is then computed from Rayleigh’s small particle limit [42] by neglecting the scattering effect,

$$\kappa_{\nu,s} = C_\nu f_s \nu, \text{ and } C_\nu = \frac{36\pi n_s k_s}{(n_s^2 - k_s^2 + 2)^2 + 4n_s^2 k_s^2} \quad (5)$$

where n_s and k_s are the wavenumber-dependent real and imaginary parts of the complex index of refraction [47].

2.2.2. Coupling strategy

In a coupled radiation-combustion simulation, the radiative source term S_r must be provided to the energy transport equation, while the RTE solver requires the local state variables, i.e, temperature, pressure, and species molar concentrations to evaluate local emissive power and absorption. Consequently, the coupling frequency between the main flow solver and the RTE solver can significantly impact the accuracy and computational cost [48]. The time step from the main hydrodynamic combustion solver is constrained by the convective time scale and by the chemical time scales. When radicals such as OH, O, and H and/or soot are considered, the chemical time scales can become the limiting time scale in fire.

For radiation, since electromagnetic waves travel at the speed of light, which can be several orders of magnitude higher than the convective velocity, the transient term in the RTE is often neglected when coupled with combustion applications. Consequently, the appropriate radiative time scale in a combustion system is determined by the dynamics of the participating species and temperature, which is correlated with the convective time scale [48]. A brief investigation of different time scales involved in this pool fire is provided below to inform the choice of updating frequency for radiation.

The convective time scale is defined as

$$\tau_{flow} = \Delta x_m/\bar{u} \quad (6)$$

where is the mean centerline axial velocity, and Δx_m is the mean grid spacing. Based on Eq. (6), the convective time scale is approximately 2×10^{-4} s. This definition was also employed in [48], where the bulk flow velocity was used for a momentum-driven flow.

The chemical time scales τ_{chem} of radiation-relevant species and soot are calculated through the eigen decomposition method. The analytical Jacobian is formulated for gaseous species and soot, and the time scales are inversely proportional to the corresponding eigen values. The time scales presented in Fig. 1 are conditional on temperature. By comparing the four species at above 1000 K, it is observed that soot chemistry is the limiting scale, which ranges from 10^{-5} to 10^{-1} s.

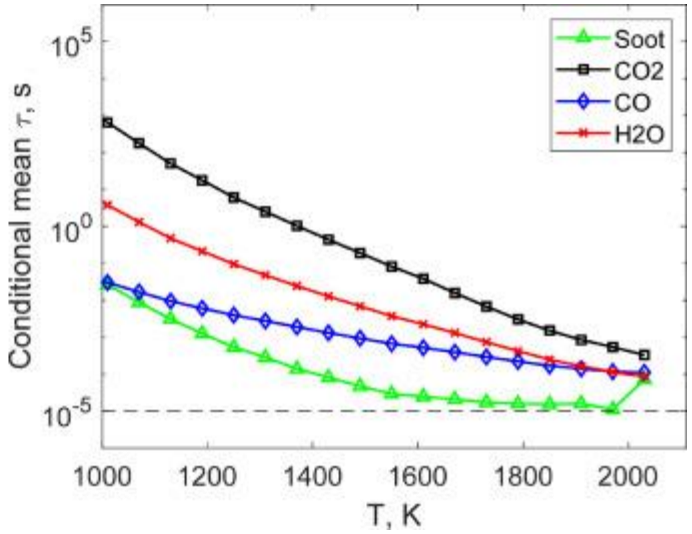

Fig. 1. Time scales of soot, CO_2, H_2O, and CO for the target pool fire.

Based on these analyses, the time step Δt for the flow solver is selected such that the chemical time scales for soot and other critical minor species are well captured. The radiative source term S_r is updated every $N_{it}\Delta t$, which is dictated by the convective time scale. Here, N_{it} is referred to as the updating frequency for radiation, and a value of 100 is used as the baseline value based on the above analyses. A comparison of the performance between a tightly-coupled simulation where $N_{it} = 1$, and two loosely-coupled simulations where $N_{it} = 100$ and 1000, is provided in Appendix B. The relative errors of global maximum temperature and total absorbed energy are within 0.3% between $N_{it} = 1$ and $N_{it} = 100$, while the relative errors between $N_{it} = 1$, and $N_{it} = 1000$, can be as large as 1.5%. Therefore, $N_{it} = 100$, is adopted in this study. The effect of the updating frequency has also been discussed in [48], [49], where $N_{it} = 100$, is also recommended. It is worth noting that the computational cost for every $100\Delta t$ is only 26% of that for the tightly-coupled simulation.

2.3. Two-equation soot model

A semi-empirical two-equation soot model [50] is coupled with the *reactingDJFoam* solver to describe soot dynamics. Two additional modeled transport equations are solved for soot mass fraction and particle number density, respectively. Particle inception, surface growth, oxidation, and coagulation are represented by the model. Inception is assumed to be based on acetylene. In addition to oxidation by O_2 [50], soot oxidation pathways are augmented by including OH and O, with the suggested reaction rates provided by [51]. Two-way coupling is employed to couple soot and gaseous species, where the concentrations of gas species are modified due to soot-related reactions. Note that one-way coupling is usually sufficient for C_2H_2-based model, as suggested by [30], [52]. Other model constants, such as the the agglomeration constant ($C_a = 9$), the density of soot ($\rho_s = 1800$ kg/m^3), the number of carbon atoms in the incipient carbon particle ($C_{min} = 100$), and the molar mass of soot ($M_s = 12.011$kg/kmol), follow the original specifications in [50]. No case-specific model parameter tuning is performed in this study.

Note that the choice of soot precursor (i.e., C_2H_2 versus polycyclic aromatic hydrocarbons (PAH)) and the chemical kinetic models can lead to large variations in the prediction of soot volume fraction, as observed in the literature [30], [31]. This aspect represents the largest uncertainty in the entire modeling framework in this study. More studies are needed to improve the fidelity of soot modeling in fire, which is left as a future research avenue.

3. Target flames

3.1. A laboratory-scale turbulent pool fire

A small (i.e., pool diameter $D = 2R_0$= 7.1 cm) heptane pool fire [10] is simulated in this study. Based on the fuel and the pool diameter, the inlet power (Q_{chem}) is 4.0 kW. The target pool fire has strong sooting propensity, leading to a significant radiant fraction (X_R) of approximately 29%. Abundant radiation-relevant experimental data are documented in [10], including the radiative heat flux along the boundaries, emissive and absorption temperatures, flame height, and radiative transmittance, etc. The flame height H_f and the inlet flow rate $\dot{m}$ are listed in Table 1. This relatively small pool size enables a detailed simulation of the flame dynamics through high-fidelity models.

Table 1. Physical and numerical parameters of the simulations.

Fuel	C_7H_{16}
Pool diameter D, cm	7.1
Inlet mass flow rate $\dot{m}$,kg/m^2 ·	0.0230
Inlet power Q_{chem}, kW	4.0
Flame height H_f, cm	34.5
Radiant fraction X_R, %	29
Domain size $R \times H$, cm	39.1 × 60
Time step Δt, µs	2
Computational cells	9.6 million
Energy rays for radiation	48 million
Kolmogorov scale (pre-estimated), cm	0.054
Kolmogorov scale (post-estimated), cm	0.057

Thermal flame thickness, cm	0.36
Soot layer thickness, cm	0.2 [56]

A cylindrical computational domain is constructed as shown in Fig. 2. The radial direction of the computational domain extends to $R = 11R_0$, where the radiative heat flux are experimentally collected. Along the axial direction, the inlet of the domain is aligned with the pool surface. Note that the fuel pan was elevated approximately 15 cm above ground level in the experiment, and the fuel level was constantly maintained at 3.5 mm below the rim of the fuel pan. These details are not captured by the current computational domain, which might have an impact on the prediction of air entrainment as discussed in similar configurations in [53]. To capture the radiation behaviors of the fire and plume, the axial span extends to approximately $1.5H_f$, or 60 cm. The resolution is approximately 0.1 cm in the axial direction and 0.05 cm in the radial direction. As shown in Fig. 2(b) from the bottom view of the computational domain, the mesh is refined at the base of the fuel inlet and stretched towards the ambient air inlet, resulting in approximately 9.6 million cells in total.

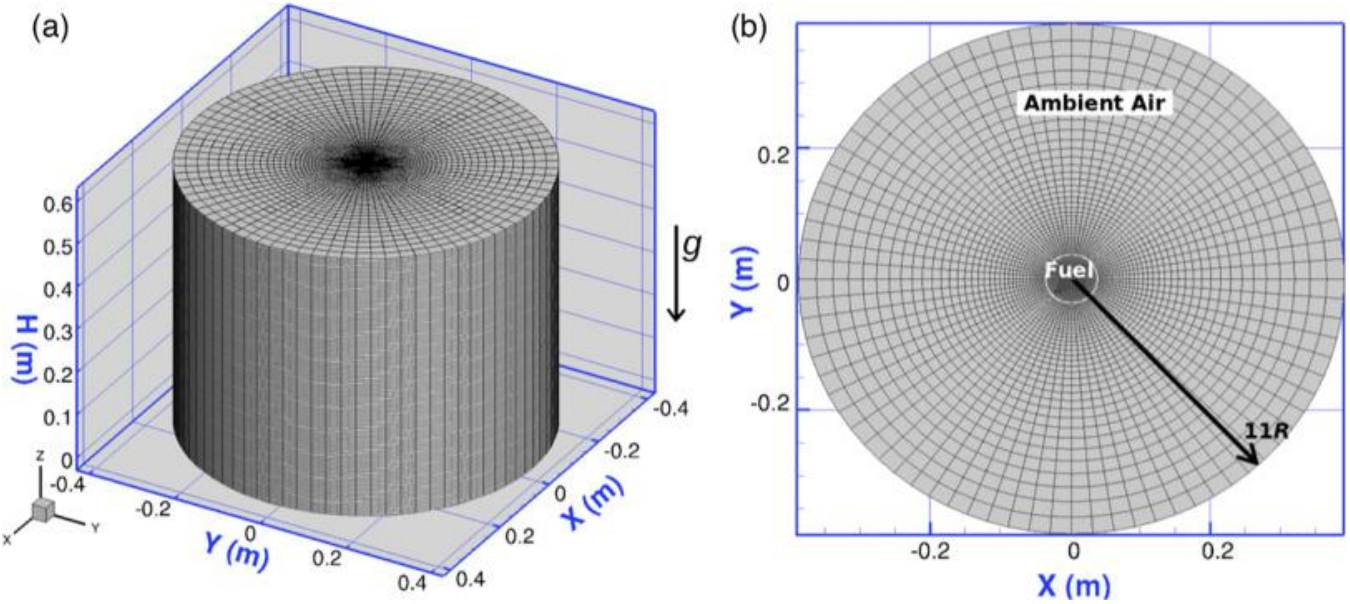

Fig. 2. Illustration of the computational domain and mesh. (a) Dimensions of the 3D computational domain. (b) Mesh details of the fuel inlet and ambient air inlet. The inner white circle indicates the rim of the pool pan.

To estimate the Kolmogorov scale for the target flame, an empirical scaling relationship [7] that relates the mean axial velocity to the fire power Q_{chem} is adopted as shown in Eq. (7a), which predicts a maximum velocity of 2.5 m/s. The fluctuating velocity is then assumed to be 30% of the maximum mean axial velocity, as shown in Eq. (7b). The integral length scale is assumed to be $L_f = 0.5D = 0.0355$ m. This results in an estimated turbulent Reynolds number of $Re_t = 267$, and an estimated Kolmogorov length scale of approximately 0.054 cm, according to Eq. (7c) for the target pool fire.

$$\bar{u}_{CL,max} = 1.9 \times Q_{chem}^{1/5} = 2.5\text{m/s} \quad (7a)$$

$$u' \approx 0.3 \times \bar{u}_{CL,max} = 0.75\text{m/s} \quad (7b)$$

$$\eta_k \sim L_f (Re_t)^{-3/4} = 0.054\text{cm} \quad (7c)$$

The laminar flame thickness δ_f is evaluated to be $\delta_f = \sqrt{D_{th,st}/\chi_{st}}$ =0.36 cm, where $D_{th,st}$ and χ_{st} are the thermal diffusivity and scalar dissipation rate evaluated at the stoichiometric location of a counterflow non-premixed flame at extinction limit. This definition of δ_f is frequently employed to assess resolution requirement for DNS of non-premixed flames [54], [55]. Based on these estimations, turbulence can be considered as resolved by the present mesh, so no sub-grid stress model is applied to the momentum equation in this simulation. Approximately seven grid cells are placed within one laminar flame thickness, and a laminar closure is adopted for the sub-grid combustion modeling in conjunction with the 33-species chemical mechanism. Based on the previous investigation of unstrained and strained laminar flames [35], we consider the laminar closure model to be adequately accurate for the grid resolution employed in the present study, especially when significant heat loss is present and prominent model uncertainty is involved with soot. The physical and numerical parameters of the simulation are summarized in Table 1.

3.2. Boundary conditions and numerical details

To avoid additional uncertainty related to the evaporation model, the liquid heptane is modeled as pre-vaporized gas with a prescribed mass flow rate. The temperature at the fuel inlet is set to be the boiling point of n-heptane at 1 atm (T_{in} = 371.6 K), while the ambient temperature and pressure are 300 K and 1 atm, respectively. All the boundaries of the computational domain are open, allowing for air to be entrained. A mixed boundary condition is assigned for velocity at the side and at the outlet of the domain, setting zero gradient for any outward flow and calculating the inlet velocity from pressure for any inward flow. A fixed total pressure condition [12] is specified at the side boundary and at the outlet of the domain. A zero-gradient boundary condition is assigned for species and temperature at the open boundaries. Note that gravity is included in the axial direction as shown in Fig. 2(a). To accurately consider the diffusive mass flux at the fuel inlet, a total mass flux boundary from the OpenFOAM library is adopted as suggested in [8]. Modifications to the total mass flux boundary are made to ensure consistency with the mixture-averaged transport property model.

The transport equations are advanced in time using a first-order implicit Euler scheme with a fixed time step $\Delta t = 2 \times 10^{-6}$s, which is determined based on discussions in Section 2.2.2. This results in a maximum Courant–Friedrich–Lewy (CFL) number of less than 0.02. Based on the time scale analysis in Section 2.2.2, the discretization error is expected to be insignificant. A second-order central difference scheme is adopted for the convective and diffusive terms.

Two cases with and without considering soot are examined and analyzed in this study, which are denoted as “Gas-soot” and “Gas-rad”, respectively. Both cases employ the same radiation solver and models. The “Gas-soot” case serves as the baseline case, while the “Gas-rad” case is constructed for parametric comparison. The baseline case is initiated with a single-step chemistry without considering radiation for the first 0.2 s to obtain a stably developing thermal flow field. Subsequently, radiation and detailed chemistry are turned on, and the solution is advanced for another 0.3 s to achieve a more realistic flame shape. After that, soot chemistry and soot radiation are initiated for the “Gas-soot” case to further advance the solution to statistically steady state. The total simulated physical time is approximately two seconds (equivalent to ten puffing periods), and statistics are collected based on the last one second.

As a postprocessing step, frozen-field analysis is employed to collect radiation relevant statistics. There, radiative source terms and fluxes are re-calculated using the same RTE solver with more statistical samples to reduce the statistical variances, while keeping the velocity, temperature and species mass fractions unaltered. It should be emphasized that the raw data analyzed in Section 4 are produced through coupled combustion-radiation simulations, hence the radiative feedback to the main hydrodynamic solver is accounted for within the dataset.

4. Results and discussions

In this section, the simulation results are first verified and validated using empirical correlations and experimental measurements. The detailed flame structures, especially in the near-pool region, are explored next. Finally, the interactions between radiation and chemistry, and interactions between gas and soot radiation are investigated in detail. Note that, unless specified otherwise, the analyses are focused on the “Gas-soot” case hereinafter.

4.1. Verification and validation

4.1.1. Puffing period and axial temperature

With limited experimental data on the flow and temperature fields, the simulation is first verified using theoretical and empirical relations for pool fires. The instantaneous axial velocity and temperature probed at $H = 0.2$ m (0.58H_f) along the centerline of the pool are presented in Fig. 3(a) to show the global flame dynamics. Strong fluctuations are observed for both axial velocity and temperature at this location, due to the unsteadiness introduced by the flame and by the buoyancy force. After Fourier transform, the power spectrum of velocity is presented in the frequency domain in Fig. 3(b). The theoretical puffing frequency is superimposed as the vertical black dashed line, which is derived to be $f = 0.5\sqrt{g/D} = 5.87$Hz (equivalent to 0.17 s in time) [57]. The prominent peak in the power spectrum of velocity is close to the puffing frequency, indicating that the most significant dynamic time scale is captured by the current simulation.

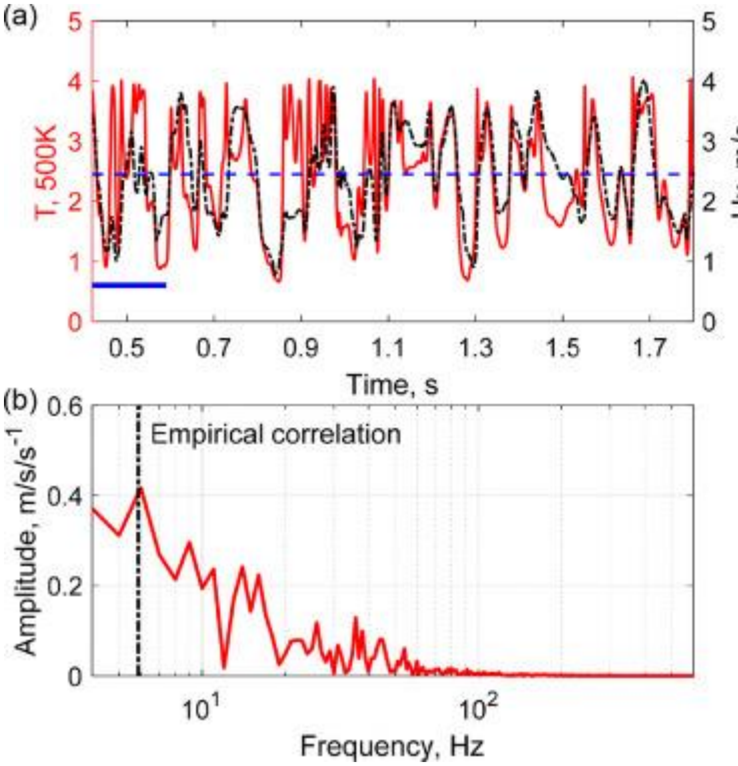

Fig. 3. (a) Transient variation of temperature (left axis) and axial velocity (right axis) at $H = 0.2$m. The blue dashed line indicates the mean axial velocity at this location. The blue solid bar indicates the duration of a puffing period. (b) Corresponding power spectrum of the axial velocity in (a). The black vertical line denotes the location of the puffing frequency.

The time-averaged temperature and axial velocity along the centerline are extracted from the last five puffing periods and are shown in Fig. 4. The vertical bars denote their respective root mean of square (r.m.s.) magnitudes. Comparison is made between the numerical solutions and empirical correlations that are derived based on experimental measurements of a collection of pool fires in [7]. Three different regions, i.e., continuous flaming, intermittent, and plume regions are separated by the vertical lines. These regions are demarcated by $H/Q_{chem}^{2/5}$ equal to 0.08 and 0.2. The mean velocity significantly rises up from zero to the maximum value within the continuous flaming region and remains relatively constant in the intermittent and plume regions in McCaffrey's correlations. The numerical results exhibit similar scaling behaviors, where close agreement is observed for both temperature and velocity in the plume region. However, in the intermittent region, large deviation between the numerical and the empirical relations is observed, which, in addition to modeling uncertainty, can be partly attributed to the fact that the empirical relations were regressed using experimental data that were heavily weighted towards 14.4 kW pool fires. In addition, the over-prediction of temperature can arise from the uncertainties in the temperature measurements, since this scaling relation was generalized from experimental data that were not corrected for thermal-couple radiation [7]. Similar discrepancy was reported in [8], where LES is coupled with an infinitely-fast chemistry model and a fixed radiant fraction model to simulate a 0.3 meter square methane pool fire. Strong temperature and velocity fluctuations are observed in the numerical results for all three regions, as indicated by the large vertical bars, and they also contribute to the discrepancy between the numerical and theoretical relations.

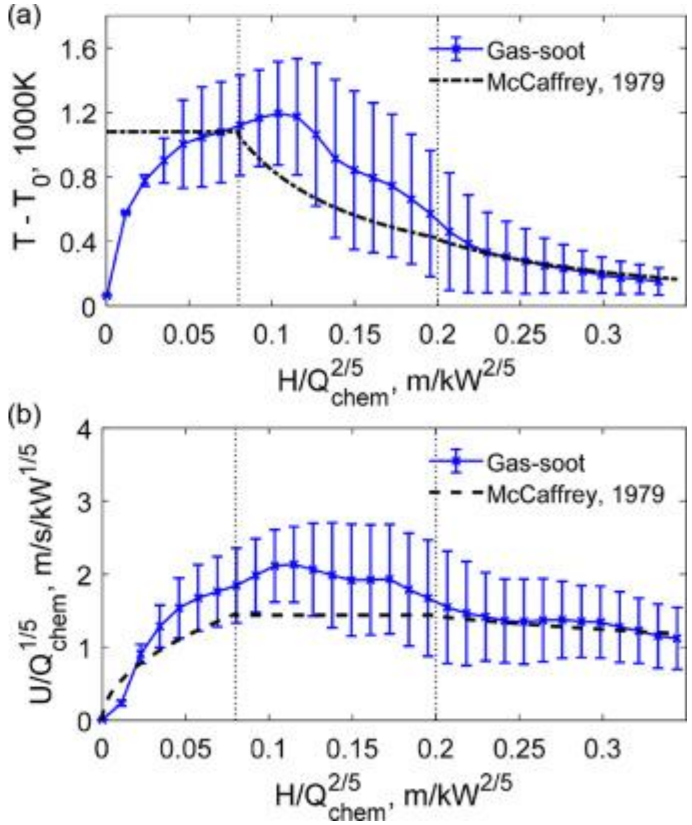

Fig. 4. A comparison of (a) mean temperature and (b) mean vertical velocity along the centerline with McCaffrey's correlations. The vertical bars denote their respective r.m.s. T_0 refers to the room temperature (300 K).

The mean turbulent velocity intensity based on the ratio of r.m.s. and mean velocities is approximately 35%. Accordingly, using Eqs. (7b) and (7c), the Kolmogorov scale (i.e., post-estimated) can be estimated again using the actual fluctuating velocity, leading to a value of 0.057 cm, which is very close to the pre-estimated value listed in Table 1. This observation confirms that the grid resolution in this study is sufficient for resolving turbulence.

4.1.2. Validation of radiative heat flux along the boundary

The radiative heat fluxes collected along the boundaries are compared with the experimental measurements in Fig. 5 to validate the simulation. The non-dimensional radiative heat fluxes, $q'' \times R^2/Q_{chem}$, are shown as a function of axial distance normalized by the flame height (H/H_f). The radial radiative heat flux is measured near the pool surface and is normalized by the square of the distance from the pool center divided by the total chemical power of the flame, $q'' \times (r - R_0)^2/Q_{chem}$. The radial distance from the pool center is normalized by the flame height, r/H_f. Frozen field analyses are performed on eight snapshots that are selected within a puffing period at a time interval of 0.02 s. The mean and r.m.s. values are not altered when sixteen snapshots are employed (not shown). Numerical results of mean and r.m.s. are then computed based on the eight snapshots, presented in Fig. 5 as lines and vertical bars. The experimental error bar is estimated based on the reported uncertainties of 20% and 40% along the axial and radial directions, respectively.

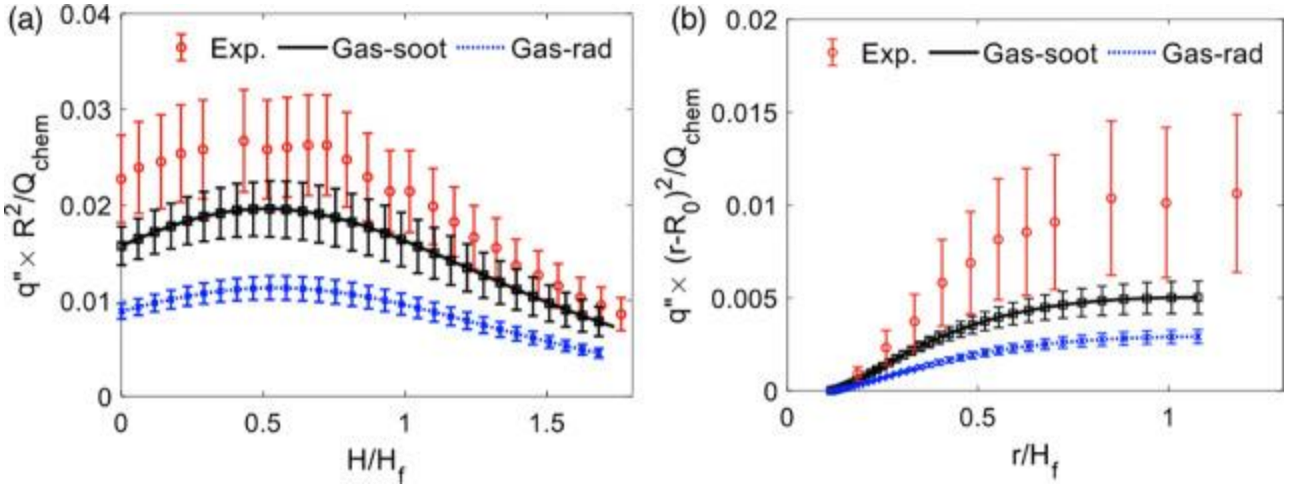

Fig. 5. A comparison of the radiative heat flux along the (a) axial and (b) radial directions. The red symbols indicate experimental results. The black and blue lines indicate results obtained with and without the soot model, respectively. (For interpretation of the references to color in this figure legend, the reader is referred to the web version of this article.)

As shown, radiative heat fluxes are significantly under-predicted when soot is ignored, as indicated by the blue dotted lines in Fig. 5. When soot is considered, the radiative heat flux shows good agreement with the experimental measurement. This suggests that soot is a non-negligible contributor to the radiative flux, which is consistent with the experimental observations [10]. The magnitude of the r.m.s of the radiative heat flux is also slightly higher in the “Gas-soot” case compared to the “Gas-rad” case, which can be caused by the intermittent thin soot structures as discussed in Section 4.2. Moreover, better agreement with the experiment is also observed for the radiative heat flux along the radial direction when soot is considered, which indicates that the existence of soot in the flame may also promote the radiative feedback to the fuel pool. As pointed out by the experimental study [10], the uncooled burner may lead to an over-prediction of the radiative heat flux near the pool. This argument possibly explains the larger discrepancy observed for the radiative flux in the radial direction.

The mean radiant fraction, which is defined using the “semi-infinite cylinder” assumption adopted in the experiment [58], is 25% based on the eight snapshots, which is 4% lower than the experimental measurement (29%). The under-prediction of radiative loss can be possibly explained by the uncertainties in predicting soot volume fractions. Figure 6 shows the radiative heat fluxes obtained from two parametric variations where the soot volume fractions are artificially increased and decreased by 50% with respect to the baseline case. The prediction obtained with 50% more soot agrees with the experiment very well along the axial direction. Improvement is also observed in the radial direction near pool. Figure 6 suggests that the current simulation potentially under-predicts soot volume fraction over the entire domain, which can lead to the under-prediction of radiative loss.

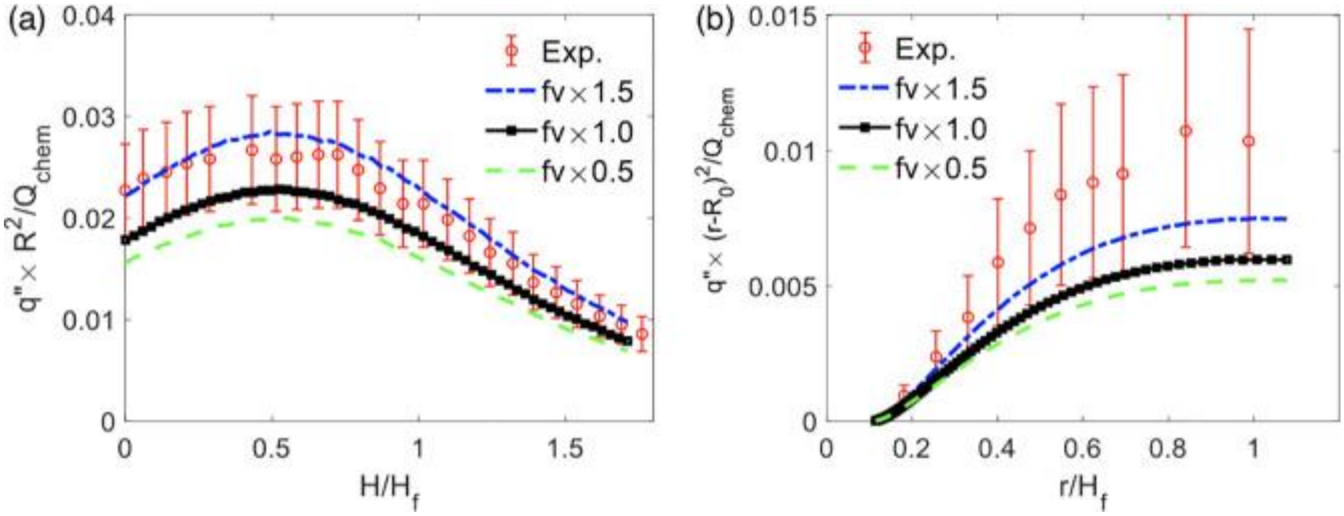

Fig. 6. A comparison of the radiative heat flux along the (a) axial and (b) radial directions. "fv × 1.5" and "fv × 0.5" respectively indicate 50% increase and decrease in soot volume fractions with respect to the baseline case (fv × 1.0).

4.1.3. Spectral flame emission

With the line-by-line spectral models, the spectral radiative flux can be extracted for comparison with experiments, as shown in Fig. 7. Consistent with the experimental measurement, the spectral radiative fluxes are collected at $r = 11R_0$ and $H/D = 1$. Statistical mean is collected from the same eight snapshots as discussed in Section 4.1.2. The r.m.s. values indicate the sample-to-sample variation in the mean spectral fluxes due to unsteadiness. Very good agreement between the computation and experiment is observed, especially at $\lambda = 4300$ nm where CO_2 emission dominates and at $\lambda = 2700$ nm where both CO_2 and H_2O emissions are significant. The good agreement in the wavelength and intensity is essentially a manifestation of the high-fidelity line-by-line spectral model and the radiation solver that are employed in this study. For wavelength smaller than 2000 nm, the emission is mostly contributed by soot, which is reflected by the broadband behavior in the spectral intensity profile. Very good agreement is observed within the range of [1000, 2300] nm, however, an experimental peak near $\lambda = 3300$ nm is missed by the computation. The wavelength range of [3268, 3512] nm suggests that the discrepancy is potentially contributed by unaccounted for C-H stretching bonds in alkanes and alkenes [59] in the combustion mixture. The conjecture is supported by Fig. 8, where the molar concentration of CH_4 is artificially increased to five and fifty folds of the predicted value. Good agreement with the experimental peak is observed when fifty folds of CH_4 is applied, although an increase of fifty folds seems to be unreasonably high.

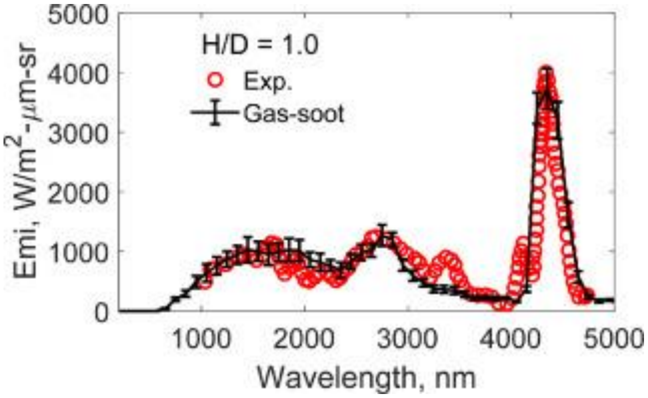

Fig. 7. Spectral radiative flux collected along line-of-sight collected at $r = 11R_0$ and $H/D = 1$ above the pool surface.

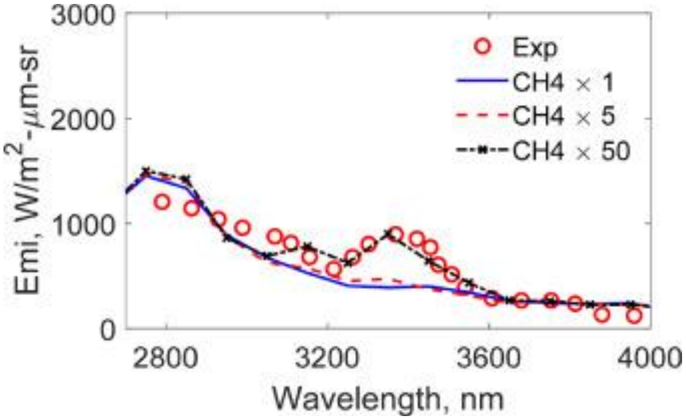

Fig. 8. Spectral radiative fluxes with different levels of CH_4 at $r = 11R_0$ and $H = 1D$ above the pool surface.

To have noticeable emission peak in the spectral intensity, the gas molecules with the C-H stretching bonds should also take on a reasonably high temperature. Clearly, the flame structure in the physical and phase spaces could provide further insights on the discrepancy, which will be discussed next in Section 4.2. With the verification and validation conducted in this section, we observe satisfactory agreement between the computation and the experiments, especially considering that no models are manually tuned to match the target condition. In particular, the radiation feature is well captured by the simulation. Subsequently, the focus will be shifted to discussions on the physical insights provided by the simulations.

4.2. Detailed flame structure and near-pool statistics

A snapshot of the instantaneous flame structure is shown in Fig. 9, where two-dimensional diametrical planes of relevant scalar fields are shown for the "Gas-soot" case. Flame sheets, indicated by the iso-line of stoichiometric mixture fraction, are observed to transition from a laminar-like smooth surface near the pool to slightly wrinkled surfaces and pinched-off pockets further downstream. Temperature and OH mass fraction (not shown) peak in the neighborhood of the stoichiometric mixture faction, indicating a typical non-premixed flame structure. The incomplete combustion product CO is concentrated inside the flame core on the fuel-rich side, while CO_2 and H_2O are distributed on both sides of the stoichiometric isoline and are convected further downstream. Soot is formed inside the flame core on the fuel-rich side as expected. The Planck mean absorption coefficient κ_P also peaks in the same region, indicating the significance of soot radiation. It should be noted that when soot is absent in the "Gas-rad" case (not shown here), κ_P is usually low along the flame sheet where temperature is high, due to the negative correlations between the gaseous absorption coefficients and temperature.

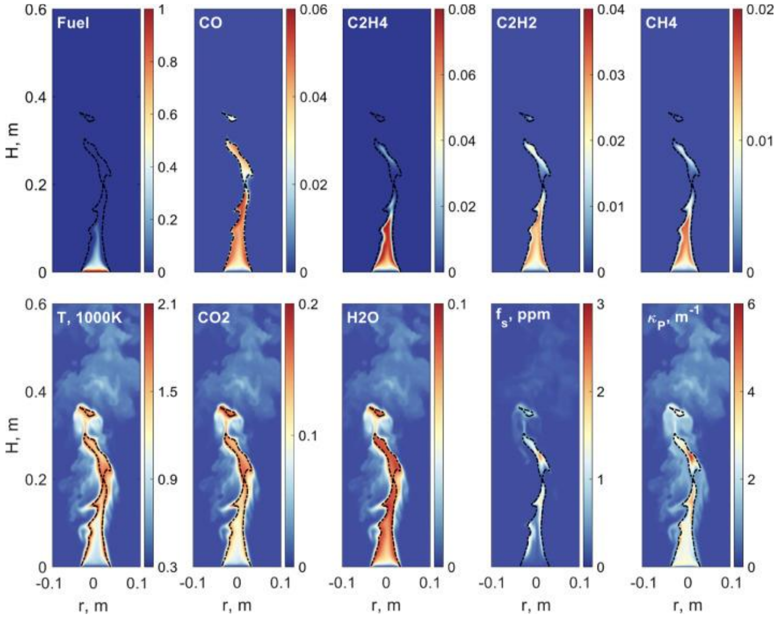

Fig. 9. Contours of instantaneous flame structures. The first row from left to right are mass fractions of fuel, CO, C_2H_4, C_2H_2, and CH_4. The second row from left to right are temperature (in 1000 K unit) and mass fractions of CO_2 and H_2O, soot volume fraction, and κ_P. The iso-line of stoichiometric mixture fraction ($Z_{st} = 0.0622$) is superimposed on each contour as the black dashed line. (For interpretation of the references to color in this figure legend, the reader is referred to the web version of this article.)

Also shown in Fig. 9, the fuel is almost depleted by $H = 0.1$ m, whereas smaller hydrocarbons still prevail. A large amount of C_2H_4 is observed within the flame core and near the flame surface, serving as the de facto fuel of the diffusion flame. Compared to C_2H_4, the mass fractions of CH_4 and C_2H_2 are much lower in this region. To further investigate the mixture composition, a top view of these species at $H/D = 1$ is displayed in Fig. 10. A few fuel cracking products are observed at this location, including C_5H_{10}, C_4H_8, C_2H_4, C_2H_2, and CH_4, with C_2H_4 being the most abundant species ($Y_{C_2H_4,max} = 0.08$). The larger hydrocarbons are more confined to the core, while the smaller hydrocarbons diffuse faster to get to the high-temperature flame sheet. Therefore, smaller molecules and radicals such as C_2H_2, C_2H_4, CH_4 and CH_2O, are more likely to contribute to the observed emissive peak in Fig. 8, compared to larger hydrocarbons such as heptane. Intermittent soot layers are formed between the stoichiometric mixture fraction and the peak C_2H_2, and concentrated in highly curved flame regions. From Fig. 9, it can be argued that more participating species need to be included in the radiation model, if the near-pool spectral radiative emission or absorption needs to be quantified. However, their contribution to overall heat loss is relatively weak.

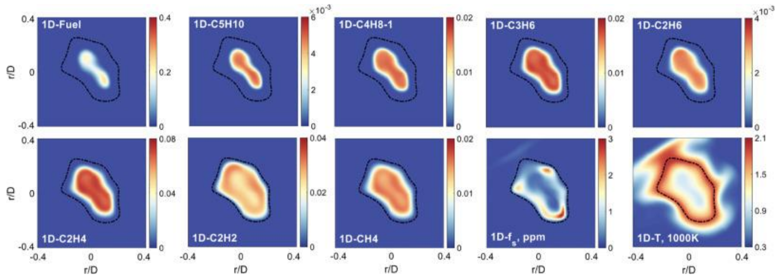

Fig. 10. Contours of instantaneous flame structures for top view at $H = 1D$. First row from left to right: mass fractions of fuel, C_5H_{10}, C_4H_8 - 1, C_3H_6, and C_2H_6. Second row from left to right: mass fractions of C_2H_4, C_2H_2, CH_4, soot volume fraction and temperature in 1000 K unit. The iso-line of stoichiometric mixture fraction ($Z_{st} = 0.0622$) is superimposed on each contour as the black dashed line. (For interpretation of the references to color in this figure legend, the reader is referred to the web version of this article.)

4.3. Radiation characteristics

4.3.1. Radiative versus chemical sources

The chemical and radiative source terms in the energy transport equation are explored to assess their respective contributions to the dynamics of sensible enthalpy. In Fig. 11, the joint probability density functions (JPDF) of the source terms and mixture fractions are collected from the same eight snapshots that are discussed in Section 4.1.2. Note only samples located within *r* ≤ 0.1 m are considered. The superimposed blue lines on the JPDFs indicate the mean values of each source term conditional on *Z*. The statistics are shown till *Z* = 0.4, beyond which both source terms are negligible. Both the “Gas-rad” and the “Gas-soot” cases are presented to understand the impact of soot on chemistry and radiation. For the “Gas-rad” case, the exothermic chemical heat release rate peaks at the flame sheet. A negative heat release zone is observed from $Z =$0.1 to $Z =$0.3, as a result of endothermic fuel cracking reactions. Note that the endothermic zone is absent when single-step chemical mechanism is employed. Peak radiative source also locates near the flame sheet and behaves as a heat sink in the energy transport equation. Similar trends of the chemical heat release rate are also observed for the “Gas-soot” case, indicating that the effect of soot chemistry is minor in changing the overall heat release behaviors. However, the peak radiative loss slightly shifts to the fuel-rich side and to higher values, due to strong soot emission induced by the high soot yield and relatively high temperature in this region. The shift of the radiation peak away from the flame sheet indicates that the radiative heat loss cannot be conveniently related to the chemical heat release rate through a constant factor.

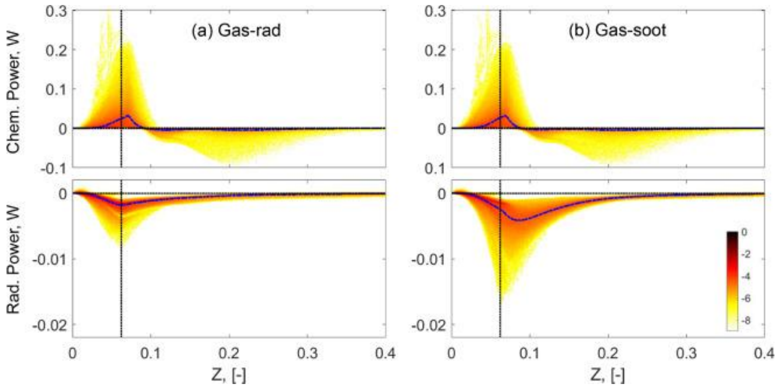

Fig. 11. JPDFs of chemical power and radiative power in the phase space for (a) “Gas-rad”, and (b) “Gas-soot” cases. The blue line indicates the conditional mean, and the black dotted line marks the stoichiometric mixture fraction.

4.3.2. Radiative interactions between gas and soot

To further distinguish radiative characteristics of gas and soot in this flame, the contributions of gas and soot to the absorption coefficient, emission and absorption source terms are investigated in the temperature space. The same eight snapshots from Section 4.3.1 are collected to obtain the Planck-mean absorption coefficients in Fig. 12 and the mean quantities in Fig. 13.

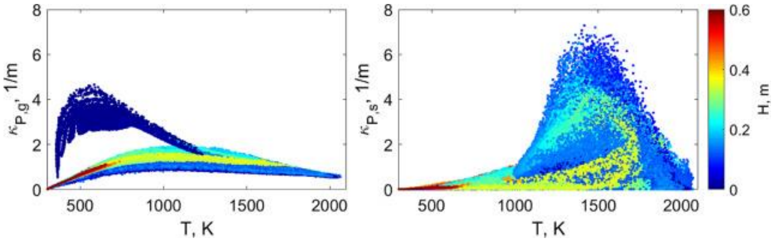

Fig. 12. Scatter plots of the Planck-mean absorption coefficients for gas (left) and soot (right) in the temperature space. The values are colored by their respective vertical locations. (For interpretation of the references to color in this figure legend, the reader is referred to the web version of this article.)

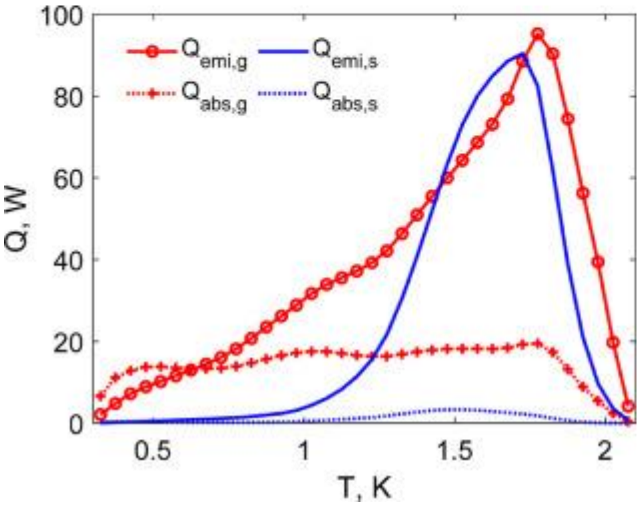

Fig. 13. Total emitted and absorbed power as a function of temperature for gas and soot, respectively.

Figure 12 shows the gaseous ($\kappa_{P,g}$) and soot ($\kappa_{P,s}$) absorption coefficients. Two branches of $\kappa_{P,g}$ are observed for the gas phase below 1200 K. The higher branch is caused by accumulated combustion products and relatively lower temperature within the flame core. Towards the flame sheet, $\kappa_{P,g}$ decreases due to the negative correlation between $\kappa_{P,g}$ and temperature. $\kappa_{P,g}$ shifts to the lower branch moving into the plume region, where CO_2 and H_2O are diluted through the entrainment of air. On the contrary, $\kappa_{P,s}$ exhibits a single peak in temperature space around 1500 K, which results from the high yield of hot soot formed inside the flame sheet (see Fig. 9). Cold soot is observed at downstream locations of the plume. The different peaks in $\kappa_{P,g}$ and $\kappa_{P,s}$ suggest that radiation behaviors by gases and soot can dominate different regions of the flame.

Figure 13 further shows the conditional mean emitted and absorbed energy as a function of temperature for gases and soot, respectively. With the T^4 dependence, emissive energy peaks in the neighborhood of 1600 to 1800 K for both gases and soot, with the peak soot emission slightly shifting to the lower temperature side due to its presence in the fuel-rich side of the flame. The total emission from the gas mixture is stronger than that from soot, i.e., at a total ratio of 3: 2. For absorption, the gaseous phase has a much stronger contribution than soot, and the gas absorption is consistently around 20 W throughout the temperature window. For temperature below 800 K, absorption exceeds emission, indicating a heating effect from radiation. Note that the total absorption is approximately 30% of the total emission in this pool fire when considering soot radiation.

4.3.3. Spectral interactions between soot and gas

With the available information on the origin of each energy ray from the radiation solver, the absorption behaviors of gas and soot are further differentiated by counting energy rays based on their emitters. As shown in Table 2, the gas absorption contributes to approximately 93% of the total absorption, and the soot absorption is only 7%, which again confirms the dominant role of gas absorption in this flame. In addition, out of the portion that is absorbed by gas, approximately 97% comes from gas emission, whereas only 3% is contributed by soot emission. This implies that self-absorption is the major mode of gas absorption. Similarly for the soot absorption, approximately 73% comes from soot, and only 27% is contributed by gas emission.

Table 2. Frozen-field analyses of the absorbed energy portion for the “Gas-soot” case. Mean absolute value within a puffing period is shown. The mean total absorbed energy is $290 + 22 = 312$ W.

	Gas absorption		**Soot absorption**	
Absorbed energy, W	**290 (93%)**		**22 (7%)**	
Emitter	**Gas**	**Soot**	**Gas**	**Soot**
Energy, W	283	7	6	16

Self-absorption from soot is slightly reduced compared to gases, which is further explained through the power spectra in Fig. 14. The emission power spectra for gases and soot are collected from the whole computational domain, as shown in Fig. 14(a). Figure 14(b) shows the power spectra collected along the boundary of the computational domain, which represents energy that reaches the boundary after being absorbed by the participative media. The wavelength distribution of CO is not shown as it only contributes to less than 2% of the total radiative energy. The distinct spectral and broadband emission behaviors from gases and soot are manifested by the intermittent and continuous emissive spectra from CO_2/H_2O and from soot, respectively. The most intensive emission occurs at a wavelength of 4300 nm, which is a signature of CO_2 emission. At 2700 nm, emission from CO_2, H_2O and soot has comparable magnitudes. For wavelengths lower than 2700 nm, soot emission is dominant.

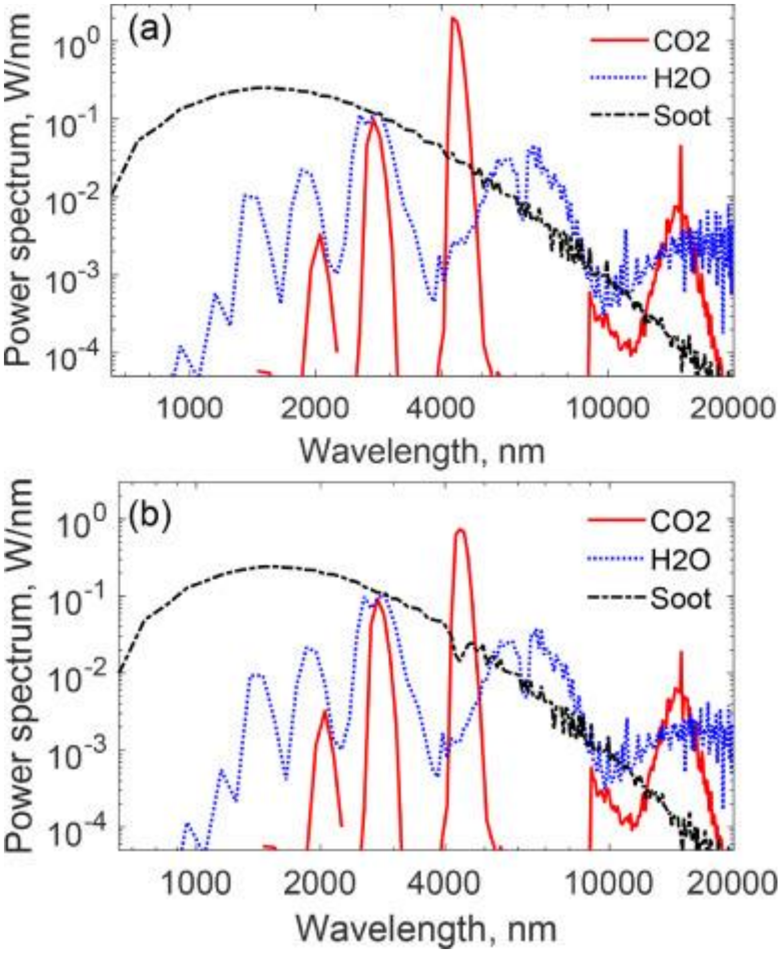

Fig. 14. Power spectra of (a) radiation emitted over the whole domain, and (b) radiative loss across the boundaries. Results are obtained from the same time instance as Fig. 9.

For the power spectra in Fig. 14(b), the magnitude of the 4300 nm CO_2 peak is reduced by 20%, due to the strong self-absorption from CO_2. Below 2700 nm, the peak power for soot, CO_2 and H_2O are not significantly reduced, indicating weaker self-absorption in this spectral window. There is a dip in the soot spectrum at 4300 nm, indicating that a discernable amount of soot emission is re-absorbed at 4300 nm by CO_2. The differences in the absorption behaviors of gas and soot can be explained by the flame structure and by their characteristic thicknesses (L_c). As shown in Fig. 9, the characteristic thickness of CO_2 layers is on the order of the pool diameter, while the characteristic thickness of soot is much smaller, on the order of a few millimeters. The optical thickness τ is proportional to the characteristic thickness (i.e., $\tau = \kappa L_c$), when the absorption coefficients are comparable between soot and gas. Consequently, the re-absorption effect is more prominent with CO_2 than with soot. In addition, the relative locations of the radiative layers also determine the amount of re-absorption. For example, soot is enclosed by hot combustion products such that soot emission at 4300 nm is clearly absorbed by the gases. On the other hand, radiation emitted from the lean side of the flame is outside the stoichiometric surface, and is largely lost to the boundary because no significant participative media exist between the outer surface of the flame and the boundary.

It is interesting to note that optically-thick and optically-thin behaviors can co-exist in a fire system. For example, the gas phase features significant re-absorption (i.e., significant optical thickness), while soot exhibits optically-thin behavior. In addition, although the overall soot radiation is optically-thin, it is optically-thick (i.e., significant re-absorption is observed) at 4300 nm because of the presence of CO_2. Such spectral interactions between gas and soot indicate the importance of accounting for the non-grey behavior when both gases and soot are contributing significantly to radiation.

5. Conclusion

A laboratory-scale turbulent heptane pool fire is simulated using a set of detailed models in this study. The turbulent flow field is captured by a turbulence-resolved mesh, finite-rate chemistry is accounted for by a 33-species skeletal mechanism, radiation is solved by a Monte Carlo ray tracing solver with a line-by-line spectral database for five participating species, and soot is modeled by a semi-empirical two-equation model. The coupled solver is developed within the OpenFOAM-4.x platform, and has been validated using a hierarchy of configurations. A transient simulation of the pool fire is conducted to fundamentally understand the interaction and coupling between chemistry, soot, and radiation. Encouraging agreement is achieved in capturing the flame temperature and vertical velocity along the axis, when comparing to the empirical scaling relations. Good agreement with experiment is achieved in predicting the radiative heat fluxes along the axial and radial directions, and the computed radiative flux is shown to be very sensitive to the prediction of soot volume fraction. With the MCRT-LBL method, the spectral distribution of the emissive power can be easily collected along a line-of-sight and directly compared with experiments. Excellent agreement with experimental data is demonstrated, especially for the 4300 μm emissive peak. Another emissive peak around 3300 nm is under-predicted by the numerical prediction, suggesting possible contributions from species that contain C-H stretching bond and are not accounted for by the current models.

The instantaneous flame structure shows peak temperature near the stoichiometric mixture faction, following a typical non-premixed flame structure. Significant fuel cracking is observed near the pool surface, with small hydrocarbon species, such as C_2H_4, acting as the de facto fuel of the diffusion flame. The total radiative re-absorption is found to be approximately 30% of the total radiative emission. Gas and soot have comparable contributions to emission, whereas gas dominates the re-absorption.

Soot significantly alters the radiative characteristics, as compared to the non-sooting condition. Soot is abundant in the fuel-rich side of the mixture, shifting the maximum Planck mean absorption coefficient from the product-abundant low-temperature downstream to the high-temperature reaction-intensive upstream of the flame. The presence of soot also shifts the peak radiative emissive power to the fuel-rich side, whereas both chemical heat release and radiative emission peak near the stoichiometric mixture fraction when soot is absent. The radiative source term is clearly disproportionate to the chemical source term, indicating that the common treatment of radiative heat source as a fixed fraction of the chemical source may fail to represent the local energy balance, especially when soot is present.

The analyses of the spectral power spectra show strong CO_2 emission and self-absorption near 4300 nm. Soot emission concentrates in the shorter wavelength range, i.e., below 2000 nm, and insignificant self-absorption is observed for soot due to its small optical thickness. Within the 4300 nm CO_2 band, a dip of the soot emssive spectra collected along the boundaries indicates strong interaction of soot and CO_2 at this wavelength. The detailed spectral power spectra in this study, for the first time, numerically quantify how soot and non-grey gases interact within pool fires. Finally, it is worth noting that the observations addressed in the present study are based on a small-scale pool fire with low levels of turbulence intensity and soot volume fraction in an open environment. Some of the conclusions are sensitive to the spatial structures of the flame. Accordingly, caution should be taken in extrapolating the results reported here to larger-scale pool fires. To simulate practical fires, it is critical and necessary to derive accurate reduced-order models with an acceptable computational cost. The insights provided by this well-resolved small-scale fire simulation will be further explored in future works to facilitate the development of such models and simulations of larger-scale fires will be performed.

Declaration of Competing Interest

The authors declare that they have no known competing financial interests or personal relationships that could have appeared to influence the work reported in this paper.

Acknowledgments

This study is partially funded by FM Global within the framework of the FM Global Strategic Research Program on Fire Modeling. The financial support from National Science Foundation (NSF1566259) is also gratefully acknowledged. The authors acknowledge helpful discussions with Dr. Prateep Chatterjee, Dr. Gang Xiong, Dr. Dong Zeng, Dr. Oluwayemisi O. Oluwole, and Dr. Yi Wang from FM Global.

Appendix A. Verification of the chemical kinetic model

To compare the performance of the skeletal mechanism on predicting species that are relevant to radiation and soot chemistry, species profiles that are obtained from a non-premixed laminar counter-flow simulation [39] are shown in the mixture fraction space in Fig. B.1. Boundary conditions of the inlet temperatures on the fuel side and the air side are the same as those used in the target pool fire simulation, and the inlet pressure is 1 atm. The global strain rate based on the inlet velocity and the computational domain length is approximately $2\ \mathrm{s}^{-1}$. Good agreement is observed for the three major radiative species. The skeletal mechanism slightly over-predicts C_2H_4 and C_2H_2 on fuel-rich side, which may slightly affect the prediction of soot dynamics. The maximum difference of the peak value of C_2H_4 is 6.8% at Z =0.234.

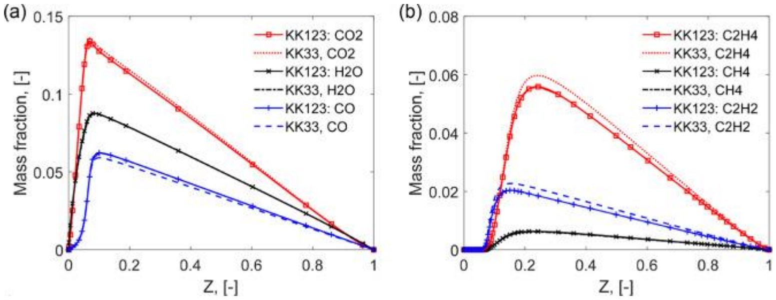

Fig. B.1. Comparisons of (a) major radiative species profiles, and (b) C_2H_4, CH_4, C_2H_2 profiles between the detailed mechanism (referred to as “KK123” [40]) and the skeletal mechanism (referred to as “KK33” [34]).

Appendix B. Effect of N_{it} in coupled radiation/CFD simulations

A comparison of the performance between the tight-coupling and loose-coupling simulations is shown in Fig. B.2. $t_{rad} = N_{it}\Delta t$, where N_{it} is referred to as the updating frequency for radiation. $N_{it} = 1$ denotes tight-coupling simulation, and $N_{it} = 100$ and 1000 denote loose-coupling simulations. As shown in Fig. B.2, negligible differences are seen for the maximum temperature, the total heat release rate, and the total absorption rate between $N_{it} = 1$ and $N_{it} = 100$. Relative errors are within 0.3% for all three variables. Larger errors are observed with $N_{it} = 1000$, where the maximum errors for total absorption is approximately 1.5%. With $N_{it} = 1000$, the coupling time scale exceeds the estimated convection time scale, which can lead to the reported discrepancy here. Therefore, $N_{it} = 100$ is adopted in this study.

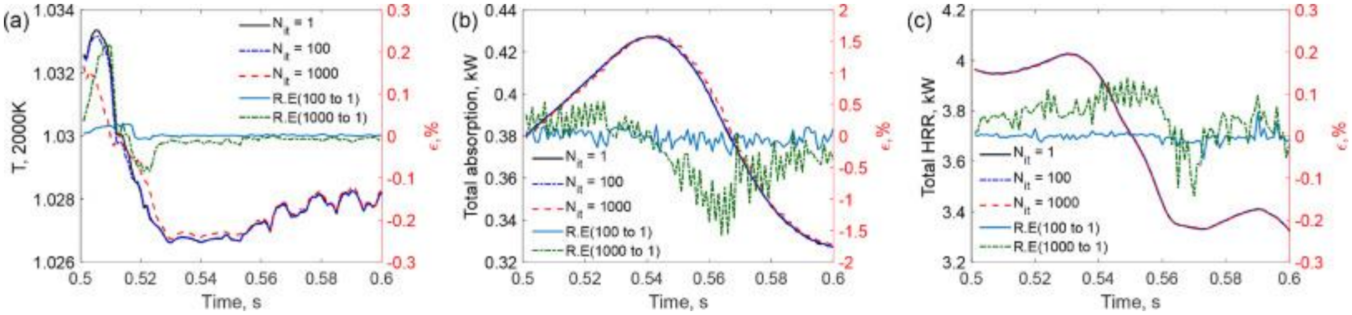

Fig. B.2. A comparison of (a) maximum temperature, (b) total heat release rate, and (c) total absorption energy rate for two updating frequencies. The left *y*-axis indicates the absolute value and the right *y*-axis indicates the relative error. (For interpretation of the references to color in this figure legend, the reader is referred to the web version of this article.)

References

[1] J.L. De Ris. **Mechanism of buoyant turbulent diffusion flames.** Procedia Eng., 62 (2013), pp. 13-27

[2] S.R. Tieszen. **On the fluid mechanics of fires.** Ann. Rev. Fluid. Mech., 33 (2001), pp. 67-92

[3] R. Viskanta. **Overview of some radiative transfer issues in simulation of unwanted fires.** Int. J. Therm. Sci., 47 (12) (2008), pp. 1563-1570

[4] B.D. Ditch, J.L. de Ris, T.K. Blanchat, M. Chaos, R.G. Bill Jr, S.B. Dorofeev. **Pool fires–an empirical correlation.** Combust. Flame, 160 (12) (2013), pp. 2964-2974

[5] M.B. Kim, Y.J. Jang, M.O. Yoon. **Extinction limit of a pool fire with a water mist.** Fire Saf. J., 28 (4) (1997), pp. 295-306

[6] S. Vilfayeau, J. White, P. Sunderland, A. Marshall, A. Trouvé. **Large eddy simulation of flame extinction in a turbulent line fire exposed to air-nitrogen co-flow.** Fire Saf. J., 86 (2016), pp. 16-31

[7] B.J. McCaffrey. **Purely buoyant diffusion flames: some experimental results.** NBSIR 79–1910 (1979)

[8] Y. Wang, P. Chatterjee, J.L. de Ris. **Large eddy simulation of fire plumes.** Proc. Combust. Inst., 33 (2) (2011), pp. 2473-2480

[9] P. Chatterjee, Y. Wang, K.V. Meredith, S.B. Dorofeev. **Application of a subgrid soot-radiation model in the numerical simulation of a heptane pool fire.** Proc. Combust. Inst., 35 (3) (2015), pp. 2573-2580

[10] M. Klassen, J. Gore. **Structure and radiation properties of pool fires.** NIST grant contract report, U.S. Department of Commerce, National Institute of Standards and Technology (1992)

[11] Y. Xin, J.P. Gore, K.B. McGrattan, R.G. Rehm, H.R. Baum. **Fire dynamics simulation of a turbulent buoyant flame using a mixture-fraction-based combustion model.** Combust. Flame, 141 (4) (2005), pp. 329-335

[12] Y.P. Almeida, P.L. Lage, L.F.L. Silva. **Large eddy simulation of a turbulent diffusion flame including thermal radiation heat transfer.** Appl. Therm. Eng., 81 (2015), pp. 412-425

[13] E. Weckman, A. Strong. **Experimental investigation of the turbulence structure of medium-scale methanol pool fires.** Combust. Flame, 105 (3) (1996), pp. 245-266

[14] G. Maragkos, T. Beji, B. Merci. **Advances in modelling in CFD simulations of turbulent gaseous pool fires.** Combust. Flame, 181 (2017), pp. 22-38

[15] G. Maragkos, T. Beji, B. Merci. **Towards predictive simulations of gaseous pool fires.** Proc. Combust. Inst., 37 (3) (2019), pp. 3927-3934

[16] J.R. Howell, K. Daun, H. Erturk. **An annotated bibliography of thermal radiation validation data for fire applications.** Report No. SAND2001-3320, Sandia National Laboratories, Albuquerque, NM, USA (2001)

[17] A. Brown, M. Bruns, M. Gollner, J. Hewson, G. Maragkos, A. Marshall, R. McDermott, B. Merci, T. Rogaume, S. Stoliarov, J. Torero, A. Trouv, Y. Wang, E. Weckman. **Proceedings of the first workshop organized by the IAFSS working group on measurement and computation of fire phenomena (MaCFP).** Fire Saf. J., 101 (2018), pp. 1-17

[18] Measurement and Computation of Fire Phenomena (2018). https://github.com/MaCFP/macfp-db.

[19] J.L. Consalvi, R. Demarco, A. Fuentes, S. Melis, J.P. Vantelon. **On the modeling of radiative heat transfer in laboratory-scale pool fires.** Fire Saf. J., 60 (2013), pp. 73-81

[20] Z. Chen, J. Wen, B. Xu, S. Dembele. **Large eddy simulation of a medium-scale methanol pool fire using the extended eddy dissipation concept.** Int. J. Heat Mass Transf., 70 (2014), pp. 389-408

[21] Y. Xin, S. Filatyev, K. Biswas, J. Gore, R. Rehm, H. Baum. **Fire dynamics simulations of a one-meter diameter methane fire.** Combust. Flame, 153 (4) (2008), pp. 499-509

[22] S.C.P. Cheung, G.H. Yeoh. **A fully-coupled simulation of vortical structures in a large-scale buoyant pool fire.** Int. J. Therm. Sci., 48 (2009), pp. 2187-2202

[23] J. Moss, C. Stewart, K. Syed. **Flowfield modelling of soot formation at elevated pressure.** Proc. Combust. Inst., 22 (1) (1989), pp. 413-423

[24] C. Fureby, G. Tabor, H. Weller, A. Gosman. **A comparative study of subgrid scale models in homogeneous isotropic turbulence.** Phys. Fluids, 9 (5) (1997), pp. 1416-1429

[25] C.W. Lautenberger. CFD simulation of soot formation and flame radiation, Worcester Polytechnic Institute (2002) Ph.D. thesis

[26] A. Snegirev, E. Markus, E. Kuznetsov, J. Harris, T. Wu. **On soot and radiation modeling in buoyant turbulent diffusion flames.** Heat Mass Transf., 54 (8) (2018), pp. 2275-2293

[27] I. Khan, G. Greeves. **A method for calculating the formation and combustion of soot in diesel engines.** Heat Transf. Flame, 25 (1974), pp. 391-402

[28] P. Tesner, T. Smegiriova, V. Knorre. **Kinetics of dispersed carbon formation.** Combust. Flame, 17 (2) (1971), pp. 253-260

[29] S. Brookes, J. Moss. **Predictions of soot and thermal radiation properties in confined turbulent jet diffusion flames.** Combust. Flame, 116 (4) (1999), pp. 486-503

[30] S.P. Roy, D.C. Haworth. **A systematic comparison of detailed soot models and gas-phase chemical mechanisms in laminar premixed flames.** Combust. Sci. Tech., 188 (7) (2016), pp. 1021-1053

[31] S.T. Chong, V. Raman, M.E. Mueller, P. Selvaraj, H.G. Im. **Effect of soot model, moment method, and chemical kinetics on soot formation in a model aircraft combustor.** Proc. Combust. Inst., 37 (1) (2019), pp. 1065-1074

[32] B. Wu, X. Zhao, S.P. Roy. **A numerical study of radiation in a small-scale pool fire.** Ninth International Symposium on Radiative Transfer, RAD-19, Begel House Inc. (2019)

[33] B. Wu, S.P. Roy, X. Zhao, M.F. Modest. **Effect of multiphase radiation on coal combustion in a pulverized coal jet flame.** J. Quant. Spectrosc. Radiat. Transf., 197 (2017), pp. 154-165

[34] T. Lu, A reduced/skeletal n-heptane models for high temperature condition (JetSurF 1.0-l) (2019). Personal communication.

[35] B. Wu, X. Zhao, B.R. Chowdhury, B.M. Cetegen, C. Xu, T. Lu. **A numerical investigation of the flame structure and blowoff characteristics of a bluff-body stabilized turbulent premixed flame.** Combust. Flame, 202 (2019), pp. 376-393

[36] OpenFOAM (2018). https://github.com/OpenFOAM/OpenFOAM-4.x.

[37] R.I. Issa. **Solution of the implicitly discretised fluid flow equations by operator-splitting.** J. Comput. Phys., 62 (1) (1986), pp. 40-65

[38] B. Wu, X. Zhao. **Coupled combustion-radiation simulations of a series of laminar non-premixed flames.** J. Quant. Spectrosc. Radiat. Transf. (2019) Under review.

[39] R.J. Kee, F.M. Rupley, E. Meeks, J.A. Miller. **CHEMKIN-II: a FORTRAN chemical kinetics package for the analysis of gas-phase chemical and plasma kinetics.** Report No. SAND96-8216, Sandia National Laboratories, Livermore, CA, USA (1996)

[40] X. You, F.N. Egolfopoulos, H. Wang. **Detailed and simplified kinetic models of n-dodecane oxidation: the role of fuel cracking in aliphatic hydrocarbon combustion.** Proc. Combust. Inst., 32 (1) (2009), pp. 403-410

[41] A. Wang, M.F. Modest. **Photon Monte Carlo simulation for radiative transfer in gaseous media represented by discrete particle fields.** J. Heat Transf., 128 (2006), pp. 1041-1049

[42] M.F. Modest. **Radiative heat transfer.** (3rd. ed.), Academic Press (2013)

[43] X.-Y. Zhao, D.C. Haworth, T. Ren, M.F. Modest. **A transported probability density function/photon Monte Carlo method for high-temperature oxynatural gas combustion with spectral gas and wall radiation.** Combust. Theor. Model., 17 (2013), pp. 354-381

[44] T. Ren, M.F. Modest. **A hybrid wavenumber selection scheme for line-by-line photon monte carlo simulations in high-temperature gases.** J. Heat Transf., 135 (8) (2013), p. 084501

[45] L.S. Rothman, I.E. Gordon, R.J. Barber, H. Dothe, R.R. Gamache, A. Goldman, V.I. Perevalov, S.A. Tashkun, J. Tennyson. **HITEMP, the high-temperature molecular spectroscopic database.** J. Quant. Spectrosc. Radiat. Transf., 111 (2010), pp. 2139-2150

[46] L. Rothman, I. Gordon, Y. Babikov, A. Barbe, D.C. Benner, P. Bernath, M. Birk, L. Bizzocchi, V. Boudon, L. Brown, A. Campargue, K. Chance, E. Cohen, L. Coudert, V. Devi, B. Drouin, A. Fayt, J.-M. Flaud, R. Gamache, J. Harrison, J.-M. Hartmann, C. Hill, J. Hodges, D. Jacquemart, A. Jolly, J. Lamouroux, R.L. Roy, G. Li, D. Long, O. Lyulin, C. Mackie, S. Massie, S. Mikhailenko, H. Mller, O. Naumenko, A. Nikitin, J. Orphal, V. Perevalov, A. Perrin, E. Polovtseva, C. Richard, M. Smith, E. Starikova, K. Sung, S. Tashkun, J. Tennyson, G. Toon, V. Tyuterev, G. Wagner. **The HITRAN2012 molecular spectroscopic database.** J. Quant. Spectrosc. Radiat. Transf., 130 (2013), pp. 4-50

[47] H. Chang, T. Charalampopoulos. **Determination of the wavelength dependence of refractive indices of flame soot.** Proc. R. Soc. Lond, 430 (1990), pp. 577-591

[48] D. Poitou, J. Amaya, M. El Hafi, B. Cuenot. **Analysis of the interaction between turbulent combustion and thermal radiation using unsteady coupled LES/DOM simulations.** Combust. Flame, 159 (4) (2012), pp. 1605-1618

[49] R.G. dos Santos, M. Lecanu, S. Ducruix, O. Gicquel, E. Iacona, D. Veynante. **Coupled large eddy simulations of turbulent combustion and radiative heat transfer.** Combust. Flame, 152 (3) (2008), pp. 387-400

[50] K.M. Leung, R.P. Lindstedt, W. Jones. **A simplified reaction mechanism for soot formation in nonpremixed flames.** Combust. Flame, 87 (3–4) (1991), pp. 289-305

[51] H. Guo, F. Liu, G.J. Smallwood. **Soot and NO formation in counterflow ethylene/oxygen/nitrogen diffusion flames.** Combust. Theor. Model., 8 (2004), pp. 475-489

[52] S.F. Fernandez, C. Paul, A. Sircar, A. Imren, D. Haworth, S. Roy, M. Modest. **Soot and spectral radiation modeling for high-pressure turbulent spray flames.** Combust. Flame, 190 (2018), pp. 402-415

[53] H. Koo, R.C. Knaus, J.C. Hewson, S.P. Domino. **Model sensitivities in LES predictions of buoyant methane fire plumes.** SAND2017-9700C, Sandia National Laboratories, Albuquerque, NM, USA (2017)

[54] V.R. Lecoustre, P.G. Arias, S.P. Roy, Z. Luo, D.C. Haworth, H.G. Im, T.F. Lu, A. Trouvé. **Direct numerical simulations of non-premixed ethylene–air flames: Local flame extinction criterion.** Combust. Flame, 161 (11) (2014), pp. 2933-2950

[55] L. Vervisch, T. Poinsot. **Direct numerical simulation of non-premixed turbulent flames.** Ann. Rev. Fluid Mech., 30 (1) (1998), pp. 655-691

[56] Y. Xin, J.P. Gore. **Two-dimensional soot distributions in buoyant turbulent fires.** Proc. Combust. Inst., 30 (1) (2005), pp. 719-726

[57] M.J. Hurley, D.T. Gottuk, J.R. Hall Jr, K. Harada, E.D. Kuligowski, M. Puchovsky, J.M. Watts Jr, C.J. Wieczorek, *et al.* **SFPE handbook of fire protection engineering.** Springer (2015)

[58] A. Hamins, M. Klassen, J. Gore, T. Kashiwagi. **Estimate of flame radiance via a single location measurement in liquid pool fires.** Combust. Flame, 86 (3) (1991), pp. 223-228

[59] E. Pretsch, P. Bühlmann, M. Badertscher. **Structure determination of organic compounds: tables of spectral data.** Springer, Berlin Heidelbergs (2009)